Tunable photocatalytic Water-splitting by the Ferroelectric Switch in 2D $AgBiP_2Se_6$ Monolayer

Lin Ju[1, 2], Jing Shang[2], Xiao Tang[2], and Liangzhi Kou[2]*

[1]School of Physics and Electric Engineering, Anyang Normal University, Anyang, 455000, China

[2]School of Chemistry, Physics and Mechanical Engineering Faculty, Queensland University of Technology, Gardens Point Campus, QLD 4001, Brisbane, Australia

KEYWORDS: Photocatalytic Water-splitting; Ferroelectric Switch; 2D Materials

ABSTRACT: Photocatalytic water-splitting is a promising technology to solve the energy crisis and provide renewable & clean energies. Recently, although numerous 2D materials have been proposed as the photocatalytic candidates, the strategies to effectively modulate photocatalytic reactions and conversion efficiency are still lacking. Herein, based on first principle calculations, we show that the photocatalytic activities and energy conversion efficiency can be well tuned by ferroelectric-paraelectric phase transition of $AgBiP_2Se_6$ monolayer. It is found that the $AgBiP_2Se_6$ monolayer has a higher potential and driving forces of photogenerated hole for water oxidation in ferroelectric phase, but the higher corresponding values of photogenerated electron for hydrogen reduction reaction in paraelectric phase. Besides, the solar-to-hydrogen energy conversion efficiency is also tunable with the phase transition, it is up to 10.04% at ferroelectric phase due to the better carrier utilization, but only 6.66% at paraelectric phase. Moreover, the exciton binding energy is always smaller in paraelectric state than that in ferroelectric state, indicating that the ferroelectric switch could also make a directional adjustment to the photo-excited carrier separation. Our theoretical investigation not only reveals the importance of ferroelectric polarization on water splitting, but also opens an avenue to modify the photocatalytic properties of 2D ferroelectric materials via ferroelectric switch.

■ INTRODUCTION

Due to the continuous growth of energy crises and environmental pollutions, photocatalysis which is a promising technology to solve these problems, has attracted significant interest in recent years. With the photocatalysts, the organic pollutants could degrade into H_2O and CO_2,[1] while H_2O can further be splitted into H_2 and O_2 molecules through redox reactions,[2-3] which is a "green" route to convert solar energy into chemical energy. Since the pioneering work of Fujishima and Honda,[4] numerous three-dimensional (3D) semiconductors have been extensively studied as photocatalysts for water splitting. Unfortunately, many of the conventional 3D photocatalysts exhibit a wide band gap, which induces a low utilization of sunlight.[5-7] Moreover, the low carrier mobilities and long migration distance in them usually causes a high recombination rate of photo-excited electrons and holes, which further shrinks its photocatalytic ability at a large level.[8]

Compared with traditional 3D bulks, 2D materials have several advantages for photocatalytic applications. They always possess large surface area, which will supply plenty of potential reactive sites. The tunable electronic structures which depend on the layer thickness and strain facilitate the optical adsorption. More importantly, the ultrathin nature and short carrier migration distance could prevent the recombination of photogenerated carriers. Therefore, the 2D materials usually possess a high photocatalytic performance. Up to now, a wide variety of 2D photocatalytic materials that have been experimentally or theoretically studied, such as graphitic carbon nitride, phosphorene, III–VI compounds, IV–VI compounds, IV–IV compounds, and transition-metal dichalcogenides (TMDs), and so forth.[9-24] Besides searching for new 2D photocatalyst materials, regulating the electron and optical properties of existing 2D photocatalyst materials to improve their photocatalytic efficiency is an alternative method, the feasible approaches include doping/adsorbing heteroatom,[13, 21, 25-29] applying tensile strain,[18, 30-32] and designing heterojunctions.[14-16, 20, 22, 33-34]

Intriguingly, polarization also could significantly affect the photocatalytic activities and water splitting efficiency since the electronic properties can be well tuned by ferroelectric polarization as demonstrated recently.[35-39] For example, the recently emerged 2D M_2X_3 (M = Al, Ga, In; X = S, Se,

Te) family and also Janus transition metal dichalcogenides have been shown to be suitable for overall water splitting due to the vacuum level difference on the two respective surfaces and the shifts of the redox potentials. The intrinsic polarization can lead to the spatial separation of photogenerated carriers.[17] Furthermore, according to the reaction mechanism proposed by Yang et al.,[40] the intrinsic dipoles help to relieve the restriction on the band gaps (1.23 eV) for water-splitting, which means that the polar semiconductors with narrow band-gap also have an opportunity to match the redox levels of water, making the photocatalytic water-splitting using visible or even infrared light possible. As analysed, the increased solar-to-hydrogen efficiency is mainly from the intrinsic spontaneous polarization. However, the effects of ferroelectric phase on photocatalysis are still unclear. To solve the issue, we investigate the effects of ferroelectric (FE) and paraelectric (PE) phases on the photocatalytic water splitting based on 2D materials ABP_2X_6 (A and B can be transition metals or rare earths atoms, and X represents the atoms from VIB group), and propose to tune the photocatalysis via ferroelectric switch. It is worthy to point out that both of the phases have been synthesized,[41-42] it will be feasible to verify the expectation from direct experimental measurements.

In this work, $AgBiP_2Se_6$ monolayer is selected for photocatalytic research due to its proper band gap, efficient light utilization and suitable band alignments relative to the redox potential of water splitting. We systematically investigate and compare their electronic and photocatalytic properties of $AgBiP_2Se_6$ under FE and PE phases for water-splitting based on density functional theory combining with G_0W_0-BSE. The result shows that the monolayer exhibits sufficient redox capacity to spilt water into H_2 and O_2. The FE $AgBiP_2Se_6$ monolayer is a high-performance photocatalyst for water oxidation while PE phase is more suitable for hydrogen reduction reaction. Remarkably, the ferroelectric switch could adjust the photo-redox capacity and the exciton binding energy. Our work demonstrate that FE-PE phase transition is a new way to modify or improve the 2D ferroelectric materials for using as a photocatalyst.

■ COMPUTATIONAL METHODS

Vienna ab initio simulation package (VASP) is selected to perform our density functional theory (DFT) calculations.[43-44] The frozen-core projector augmented wave (PAW) and the generalized gradient approximation (GGA) approximation are chosen to describe the interaction between the valence and core electrons.[45-47] The electronic structures are assessed using the Heyd–Scuseria–Ernzerhof (HSE06)[48] hybrid functional to avoid the underestimate of the band gap calculated within Perdew–Burke–Ernzerhof (PBE) functional. Normal to the sheets, a 20 Å vacuum space is applied to the layers. The long-range vdW interactions between layers are described within a dispersion correction of total energy (DFT-D3 method) was used to incorporate the long-range vdW interaction.[49] For the asymmetric layer arrangement, the dipole correction is considered. The cutoff energy is 500 eV. For the 2D Brillouin zone sampling, 5 × 5 ×1 Monkhorst–Pack k mesh is chosen. The geometrical structure relaxations are carried out until the residual force and energy difference are, respectively, less than 0.02 $eVÅ^{-1}$ and 10^{-5} eV. When calculating the Gibbs free energy of hydrogen reduction and water oxidation reactions, we consider the solvent effect by using the implicit water solvent model implemented in VASPsol.[50-51]

■ RESULTS AND DISCUSSION

To comprehensively understand the effects of ferroelectric phase on the photocatalytic performance of water splitting, we study and compare the detailed differences of electronic properties, spectrum adsorption, band alignments, water adsorption strength and driving force of photo-exited carriers at different phases.

Structure, electronic properties and optical adsorption at FE and PE phases. Before the discussions of photocatalytic properties of $AgBiP_2Se_6$, we first compare the corresponding structural, electronic and optical adsorption differences at FE and PE phases respectively, as the foundations to understand different photocatalytic behavior. Monolayer $AgBiP_2Se_6$ is constituted by a P–P in a triangular pattern and chalcogenide framework with the octahedral sites filled by Ag and Bi atoms. As illustrated in Figure 1a, Ag and Bi atoms are all located in the middle plane for the PE phase. However, the Ag^+ ion is shifted off-center along z direction in the ferroelectric ordering, the displacement is much larger than that of the Bi^{3+} ion, therefore generating a spontaneous polarization of 0.28 Debye vertical to the monolayer. From the calculated total energy, the FE phase of monolayer $AgBiP_2Se_6$ is energetically 33 meV lower than the PE one, which is consistent with the previous reports like that of $CuInP_2S_6$ monolayer.[41] It also means that it is relatively easy to achieve the ferroelectric switch from PE to FE phase or vice versa. Due to the presence of structural asymmetry, the lattice parameter is also slightly different as listed in Table 1, the value is 6.714 Å at PE phase, but 6.696 Å at FE phase. These results match well with the previous report (6.69 Å for the FE $AgBiP_2Se_6$ monolayer).[52]

The structural difference at two phases will lead to the shift of energy levels and spectrum adsorptions. Based on HSE06 methods, the band structures of the PE and FE phase $AgBiP_2Se_6$ monolayer are calculated. Due to the heavy Bi atom, the spin-orbital coupling (SOC) correction is also examined with the HSE06 functional. The effect of SOC on the indirect band gaps of FE and PE phase $AgBiP_2Se_6$ monolayers are 0.14 and 0.18 eV, respectively, which is small relative to their own indirect band gaps (displayed in Figure S1). Considering the huge computational cost, we do not apply the SOC correction in the following calculation. As shown in Figure 1c and 1d, the band structures present similar features beside the values of band gaps and the positions of band-edge states. It can be seen that both PE and FE phase $AgBiP_2Se_6$ are

semiconductors with indirect band gap. The conduction band minimum (CBM) and valence band maximum (VBM) of PE $AgBiP_2Se_6$ is separately located at Γ and K point, but they are located at Γ point and Γ-K path in FE $AgBiP_2Se_6$, respectively. Furthermore, as illustrated in Figure S2, for both phases, the main contributions of the CBM of $AgBiP_2Se_6$ are *p* orbitals of Se and Bi atoms, meanwhile the VBM is dominated by the hybridization of Ag *d* orbital and Se *p* orbital. At HSE06 level, the indirect band gaps of FE phase $AgBiP_2Se_6$ is 2.25 eV which is in accordance with the previous results (2.31 eV for FE $AgBiP_2Se_6$, [52-53]). In contrast, the band gap value of $AgBiP_2Se_6$ is reduced to 2.20 eV at PE phase. As listed in Table S3, we also calculated the electronic properties of $CuBiP_2Se_6$, $CuInP_2S_6$ and $AgBiP_2S_6$ monolayers, it is found that the $E_g^{d(HSE)}$ of FE phase are generally larger than the one in the PE phase. The decrease of band gap accompanied with FE-to-PE phase transition also has been observed in $CuCrP_2S_6$, $CuCrP_2Se_6$, $CuVP_2S_6$, and $CuVP_2Se_6$.[42] In addition, for both phases of $AgBiP_2Se_6$ monolayer, the band gaps are larger than 1.23 eV, meeting the basic requirement of water splitting, namely the gap value is larger than the difference between the redox potentials of H^+/H_2 and H_2O/O_2

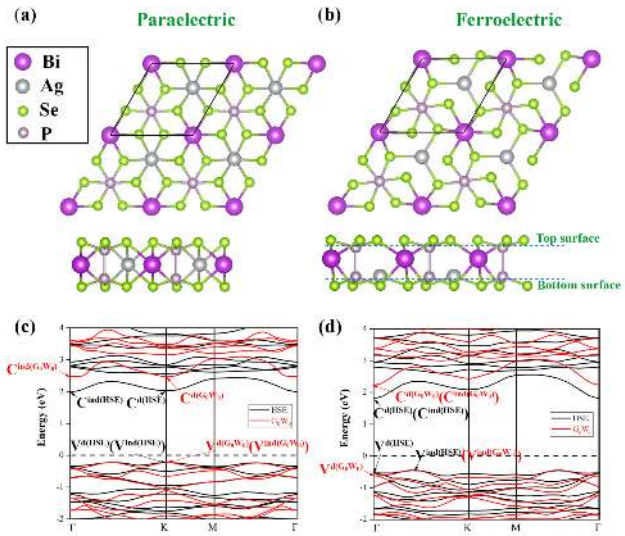

Figure 1 Crystal structure of (a) paraelectric and (b) ferroelectric $AgBiP_2Se_6$ monolayer. Band structures of (c) paraelectric and (d) ferroelectric $AgBiP_2Se_6$ monolayers based on HSE06 (black line) and G_0W_0 (red line) functional. The Fermi levels are set as 0 eV.

We confirmed the band gaps of $AgBiP_2Se_6$ monolayers using the G_0W_0 method, since the calculations for optical adsorption will base on the approach. As shown in Figure 1c and 1d, we can see that the indirect band gaps of PE $AgBiP_2Se_6$ monolayers is 2.68 eV, while the FE one is 2.70 eV. Notably, the energy differences between direct and indirect band gaps for the FE $AgBiP_2Se_6$ monolayers (80 meV) is larger than the thermal energy at room temperature (KT~30 meV),[17] which can effectively prevent the combination of photo-exited carriers. The VBM is higher than the top valence bands at the Γ point, and the excited electrons could jump from valence band to conduction band at Γ point and then the holes move from Γ point to VBM, realizing the separation of photo-generated carriers.

As an efficient photocatalyst, the optical absorption coefficient should be strong, which gives rise to photo-excited electron–hole pairs. Here, we investigate the optical absorbance [$a(\omega)$] and imaginary parts of dielectric function (ε_2) with G_0W_0-BSE method, the results are displayed in Figure 2 and S3. The absorbance is calculated by following equation:[17, 54]

$$a(\omega) = \sqrt{2}\omega\left(\sqrt{\varepsilon_1(\omega)^2 + \varepsilon_2(\omega)^2} - \varepsilon_1(\omega)\right)^{\frac{1}{2}} \quad (1)$$

Under visible-light region, the optical absorption spectrum shows that $AgBiP_2Se_6$ monolayer exhibit an obviously high optical absorbance, indicating it is a potential photocatalyst with visible light response. Moreover, it is found that although the optical adsorption of FE $AgBiP_2Se_6$ at the range of green to red light region was suppressed to some degree, it is significantly increased at the ultraviolet light area when compared with the PE phase. The results imply that the optical adsorption can be also modulated by the ferroelectric switch or phase transition.

Table 1 Optimized Lattice Constants (*a*), Band Gaps (direct and indirect) at HSE06 and G_0W_0 level, the Optical Band Gaps (E_{opt}), Exciton Binding Energies (E_b), Dipole Moments (μ), and Difference of Electrostatic Potential (ΔV) between Top and Bottom Surfaces for Paraelectric and Ferroelectric $AgBiP_2Se_6$ Monolayers.

	a (Å)	$E_g^{ind(HSE)}$ (eV)	$E_g^{d(HSE)}$ (eV)	$E_g^{ind(GW)}$ (eV)	$E_g^{d(GW)}$ (eV)	E_{opt} (eV)	E_b (eV)	μ (Debye)	ΔV (eV)
$AgBiP_2Se_6$ (PE)	6.714	2.20	2.25	2.68	2.70	2.23	0.47	0	0
$AgBiP_2Se_6$ (FE)	6.696	2.25	2.33	2.70	2.86	2.23	0.63	0.28	0.27

The binding energy of excitons is an important factor to separate photo-excited carriers, which is defined as:

$$E_b = E_q - E_{opt} \quad (2)$$

where E_q is the quasi-particle band gap obtained based on the GW method (corresponding to $E_g^{d(GW)}$) and E_{opt} is the energy corresponding to the initial peaks of the optical absorption. The exciton binding energy is displayed in Table 1, basically following the law of $E_b \approx E_q/4$.[55-56] It can be seen that the FE $AgBiP_2Se_6$ monolayer has a larger exciton binding energy than PE one. In order to confirm the law above, we also calculate the exciton binding energy of monolayer $AgBiP_2S_6$, $CuBiP_2Se_6$ and $CuInP_2S_6$. More computational details can be found in Figure S3 and S4. As listed in Table S1, all these three cases also follow the law, indicating that the ferroelectric switch is indeed an effective and universal way to regulate the exciton binding energy of ABP_2X_6 (A = Ag, Cu; B = Bi, In; X = S, Se) system. In addition, the small exciton binding energy (smaller than the one of most MXene monolayers[56]) is favourable for the separation of photogenerated carriers.

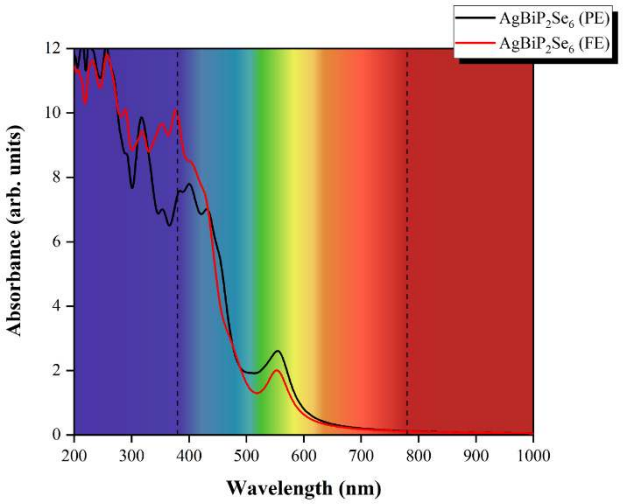

Figure 2 Optical absorption coefficients of paraelectric and ferroelectric $AgBiP_2Se_6$ monolayers. The scale of the visible light region (380~780 nm) is in iridescent color.

Band Alignment. Owing to the broken mirror symmetry, there is an intrinsic dipole moment for FE $AgBiP_2Se_6$ monolayers, which generate a built-in electric field perpendicular to the layer. The direction of built-in electric field pointing from bottom surface to up surface, and the electrostatic potential difference is 0.27 eV (as illustrated in Figure 3b). To explore the spatial distribution of carriers further, we investigate the partial charge density of CBM and VBM for both FE and PE $AgBiP_2Se_6$ monolayers, which are presented in Figure 3c and 3d, respectively. For the PE phase, both VBM and CBM uniformly spread over both surfaces. So, the reactivities of oxygen evolution reaction (OER) and hydrogen evolution reaction (HER) are the same at both surfaces. In contrast, for the case of FE phase, the VBM mainly distribute at the top surface and the CBM at the bottom surface. Under the action of built-in electric field, the photo-excited electrons incline to distribute at the top surface, while the holes tend to distribute at bottom surface. As a result, HER will probably mainly occurs at the bottom surface, while OER at the top surface, which would effectively decrease the carrier recombination and increase the photocatalytic efficiency.

For an overall water splitting photocatalyst, the potential of the CBM should be higher than the reduction level of hydrogen (-4.44 eV at pH = 0), and the potential of the VBM should be lower than the oxidation level of oxygen (-5.67 eV at pH = 0). As shown in Figure 3, for both PE and FE $AgBiP_2Se_6$ monolayers, the VBM and CBM surpass the standard oxidation potential of H_2O/O_2 and the standard reduction potential of H^+/H_2, indicating their sufficient activity for both OER and HER, respectively. According to the previous literature,[34, 57] we define the potential of photogenerated electrons for hydrogen reduction reaction (U_e) as the energy difference between the hydrogen reduction potential and the CBM, while the potential of photogenerated holes for water oxidation (U_h) is calculated as the energy difference between the hydrogen reduction potential and the VBM. The reduction potential ($E^{red}_{H^+/H_2}$) changes with the pH according to:

$$E^{red}_{H^+/H_2} = -4.44 + \mathrm{pH} \times 0.059 \ (\mathrm{eV}) \qquad (3)$$

At pH = 0, U_e is 0.68 eV and U_h is 1.52 eV for PE phase $AgBiP_2Se_6$. At the bottom surface of FE phase $AgBiP_2Se_6$, U_e is 0.50 eV. According to the Yang's theory,[58] at the top surface of FE phase $AgBiP_2Se_6$, the reduction potential ($E^{red}_{H^+/H_2-top}$) would rise with the electrostatic potential difference ($\Delta\Phi$) as:

$$E^{red}_{H^+/H_2-top} = E^{red}_{H^+/H_2} + \Delta\Phi \qquad (4)$$

So, the U_h for the top surface FE phase $AgBiP_2Se_6$ is 2.29 eV. In the neutral environment (pH = 7), based on the Equation 3, the U_e and U_h for PE phase $AgBiP_2Se_6$ monolayer is 0.27 and 1.93 eV, respectively. In contrast, the U_e at the top surface and U_h at the bottom surface for FE phase $AgBiP_2Se_6$ is 0.09 and 2.70 eV, respectively. The positive U_e and U_h indicate both PE and FE phase $AgBiP_2Se_6$ monolayers potentially have photocatalytic activity for water-splitting in the neutral environment. For practical application, we also evaluate the stability of photocatalysts in the aqueous solution under illumination. According the method proposed by Chen *et al.*,[59] the thermodynamic oxidation potential (ϕ^{ox}) and reduction potential (ϕ^{re}) of PE and FE $AgBiP_2Se_6$ monolayers are calculated, respectively. More computational details can be found in the *Supporting Information*. As displayed in Figure 3a and 3b, the ϕ^{ox} of both PE and FE $AgBiP_2Se_6$ monolayers (red line) are lower than the oxidation potential for O_2/H_2O, while both the ϕ^{re} (blue line) are higher than the reduction potential for H^+/H_2, which reveals that photogenerated carriers prefer to react with water molecule rather than the photocatalysts themselves.[59] Hence both PE and FE phase $AgBiP_2Se_6$ monolayers have a good resistance to photoinduced corrosion. Notably, in monolayer $AgBiP_2Se_6$, the PE phase

has a stronger reducibility and the FE phase processes a higher oxidizability, which demonstrates that the ferroelectric switch could tune the redox abilities of ferroelectric catalyst.

Energy Conversion Efficiency. We then estimate the energy conversion efficiency of monolayer $AgBiP_2Se_6$ for photocatalytic water splitting. The method is presented in the *Supporting Information*. To check the efficiency of the catalytic reaction,[60] the energy conversion efficiency of light absorption (η_{abs}), carrier utilization (η_{cu}), solar-to-hydrogen (STH) (η_{STH}) and corrected STH (η'_{STH}) are listed in Table 2. Although light adsorption efficiency η_{abs} in PE phase (26.04%) is slightly higher than FE phase (23.12%), FE phase has a much higher carrier utilization efficiency η_{cu} (44% vs 25.59%) due to the effective electron-hole separation as a result of intrinsic electric field. Therefore, the STH efficiency (η_{STH}) which can evaluate the additional energy required to surmount the barriers of the HER and OER is obviously larger at FE phase (10.27%) compared with PE phase (6.66%). With the polarization in consideration, the corrected STH efficiency of FE $AgBiP_2Se_6$ monolayer can still reach up to 10.04%, which is the highest among the family of ABP_2X_6 (A = Ag, Cu; B = Bi, In; X = S, Se) materials we considered (as listed in Table S2). One can see that their energy conversion efficiencies also can be well regulated by ferroelectric-paraelectric phase switch.

Table 2 Energy conversion efficiency of light absorption (η_{abs}), carrier utilization (η_{cu}), STH (η_{STH}) and corrected STH (η'_{STH}) of Paraelectric and Ferroelectric $AgBiP_2Se_6$ Monolayers.

	η_{abs} (%)	η_{cu}(%)	η_{STH}(%)	η'_{STH}(%)
$AgBiP_2Se_6$ (PE)	26.04	25.59	6.66	--
$AgBiP_2Se_6$ (FE)	23.12	44.40	10.27	10.04

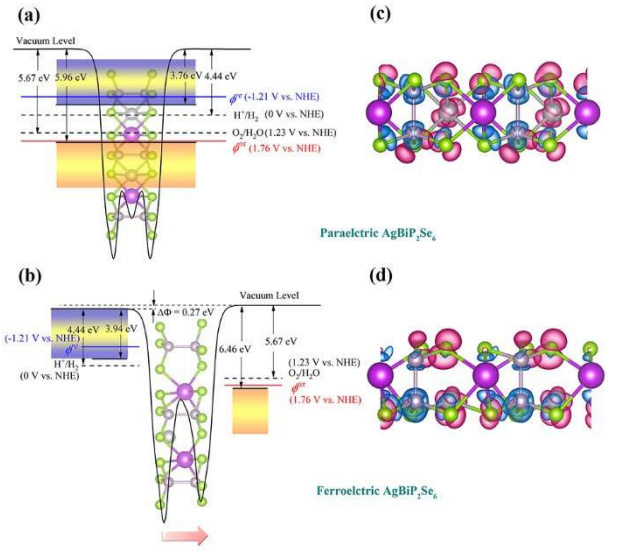

Figure 3 Band edge positions with respect to water redox potential for paraelectric (a) and ferroelectric (b) $AgBiP_2Se_6$ monolayers based on the HSE06 functional. Blue and purplish red bars represent the positions of CBM and VBM, respectively. The black dashed line represents the redox potential of water splitting at pH = 0. The blue and red lines represent the thermodynamic oxidation potential (ϕ^{ox}) and reduction potential (ϕ^{re}), respectively. The pink arrow marks the direction of intrinsic dipole. The charge distribution of paraelectric (c) and ferroelectric (d) $AgBiP_2Se_6$ monolayers for the states relative to the CBM and VBM denoted with blue and red color, respectively. The value of isosurface is set as 0.006 e/Å^3.

Adsorption of Water Molecule. We then valuate the effects of FE phase transition on the photocatalytic water-splitting capacity. As the first and key step, the adsorption behavior of H_2O on the $AgBiP_2Se_6$ monolayer will be studied and compare the differences for FE and PE phases. For PE $AgBiP_2Se_6$ monolayer, the two sides are the same, so we only investigate one surface (labeled as PE-H_2O). For FE $AgBiP_2Se_6$ monolayer, the adsorptions on the top and bottom surfaces are both studied (labeled as FE(top)-H_2O and FE(bottom)-H_2O, respectively). As displayed in Figure S5, different adsorption sites for H_2O are considered to explore the most stable adsorption configuration. After geometrically optimized, the most energetically stable adsorption structures of H_2O are identified on the $AgBiP_2Se_6$ monolayer. On the PE $AgBiP_2Se_6$ monolayer surface, the O atom of the absorbed H_2O molecule locates above near the hexagonal center of the lattice and the vertical distance between the H and Se layer is about 1.97 Å. On the top surface of FE $AgBiP_2Se_6$ monolayer, the O atom stays above the Ag atom with 2.27 Å between the H and Se layer, while on the bottom surface, it is located above the Bi atom and the vertical distance between the H and Se layer is 2.01 Å. In order to estimate the interaction strength between the H_2O molecule and the $AgBiP_2Se_6$ monolayer, we defined the adsorption energy (E_{ads}) as following equation:

$$E_{ads} = E_{total} - E_{layer} - E_{H_2O} \qquad (5)$$

where E_{total} is the total energy of the whole gas-adsorbed system, E_{layer} corresponds to the energy of the pristine $AgBiP_2Se_6$ monolayer and E_{H_2O} is the energy of the isolated H_2O molecule. We find that all the E_{ads} values for the three case are negative and they are in the order of $E_{ads(FE(top)-H_2O)}(-0.448\ eV) > E_{ads(PE-H_2O)}(-0.466\ eV) > E_{ads(FE(bottom)-H_2O)}(-0.480\ eV)$. Usually, the adsorbed molecule can be stabilized by the charge transfer. Based on the Bader analysis, as plotted in Figure S6, we find there are a total of 28.42×10^{-3}, 28.64×10^{-3} and 44.49×10^{-3} electron transferring from $AgBiP_2Se_6$ monolayer to adsorbed H_2O molecule, which is consistent with the result of adsorption energy in these three cases. The difference of the electron transferring on the two surfaces of FE $AgBiP_2Se_6$ monolayer may be due to the electric potential difference. As

illustrated in Figure 3b, due to the instinct electric filed, the bottom surface has a lower electric potential than the top surface, so the electron could transfer to the adsorbed H_2O molecule more easily. The results of electron transfer also in turn confirm the validity of the direction of the built-in electric field in FE $AgBiP_2Se_6$ monolayer.

Driving Force of Photo-exited Carriers for Overall Water Splitting. In order to explore the effect of ferroelectric switch on the driving force of photogenerated electrons and holes of $AgBiP_2Se_6$ monolayer, we finally systematically investigated mechanisms of both water oxidation and hydrogen reduction under the PE and FE phases, respectively.

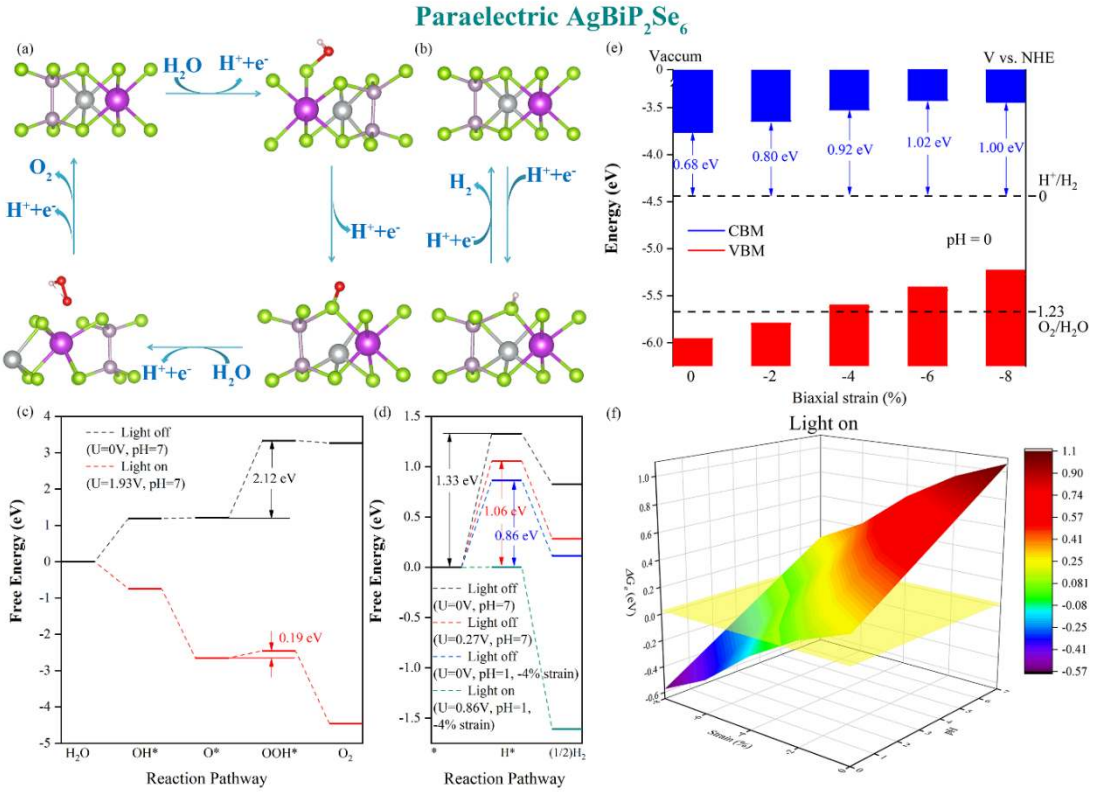

Figure 4 Proposed photocatalytic pathways of water oxidation **(a)** and hydrogen reduction **(b)** half reactions with the most energetically favorable absorbed intermediates (OH*, O*, OOH*, and H*) in paraelectric $AgBiP_2Se_6$ monolayer. The red and green balls represent O and H atoms, respectively. Free energy diagrams of OER **(c)** and HER **(d)** on paraelectric $AgBiP_2Se_6$ monolayer under different conditions. The CBM and VBM of paraelectric $AgBiP_2Se_6$ monolayer under different biaxial compression strains (e). ΔG_e of paraelectric $AgBiP_2Se_6$ monolayer versus different applied biaxial compression strains and pH (f). The optimal reaction barrier (25 meV) is highlighted in yellow plane.

As illustrated in Figure 4a and 5a, the half reaction of water oxidation follows a four-electron (4*e*) reaction pathway, accompanied by the intermediate product of OH*, O*, and OOH*. The corresponding free-energy profiles for PE and FE phase $AgBiP_2Se_6$ monolayers are separately summarized in Figure 4c and 5c, where the black lines represent the situation without any external potential to simulate the condition in the absence of any light irradiation (U = 0V). More computational details can be found in the *Supporting Information*. On the surface of PE $AgBiP_2Se_6$, the adsorbed water molecule is firstly transformed into a *OH species with a ΔG of 1.19 eV; Secondly, after releasing an electron and a proton, the *OH species is oxidized to O* species, with a ΔG of 0.02 eV; Thirdly, combining with another water molecule, *O species is oxidized to OOH* species with a ΔG of 2.12 eV, which is the highest free energy change in the water oxidation half reaction; Finally, the OOH* species spontaneously liberate a free O_2 molecule, a proton and an electron, releasing the heat of 0.07 eV. The water oxidation half reaction on the top surface of FE phase $AgBiP_2Se_6$ monolayers is similar to that of PE phase, but with different reaction barriers. The ΔG for 1~4 step is 1.24, -0.07, 2.17 and -0.08 eV, respectively. For both phases, the water oxidation half reactions are not energetically favorable on the surface of $AgBiP_2Se_6$ monolayer without light irradiation.

As shown in Figure 4c and 5c, when the $AgBiP_2Se_6$ monolayers under illumination, an external potential will be provided by photogenerated holes (U=1.93 and 2.70 V for PE and FE $AgBiP_2Se_6$ monolayers, respectively). Remarkably, all the steps are downhill in the FE case, indicating that, FE $AgBiP_2Se_6$ monolayer has the ability of catalyzing water oxidation in the neutral condition under

illumination. More notably, as shown in Figure S7, under illumination, the ferroelectric $AgBiP_2Se_6$ monolayer could oxidize water into oxygen spontaneously even in the acid medium ($3 \leq pH < 7$), which can't be done for most existing photoelectrocatalysts, because of the high overpotential and instability.[61] As for the case of PE phase, the third step is still uphill (ΔG = 0.19 eV), indicating the O* species cannot be transformed into OOH* species spontaneously, namely the OER reaction can't be achieved even under the light illumination. Therefore, the ferroelectric switch could adjust the driving force of photogenerated holes of $AgBiP_2Se_6$ monolayer to water oxidation and FE $AgBiP_2Se_6$ monolayer could be a potential photocatalyst for OER.

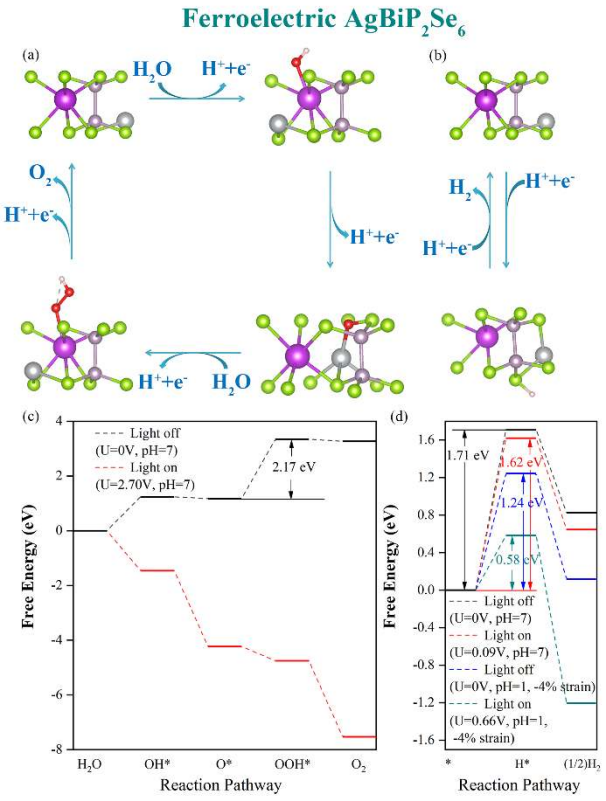

Figure 5 Proposed photocatalytic pathways of water oxidation **(a)** and hydrogen reduction **(b)** half reactions with the most energetically favorable absorbed intermediates (OH*, O*, OOH*, and H*) in ferroelectric $AgBiP_2Se_6$ monolayer. The red and green balls represent O and H atoms, respectively. Free energy diagrams of OER **(c)** and HER **(d)** on ferroelectric $AgBiP_2Se_6$ monolayer under the different conditions.

As for the hydrogen reduction half, there are only two steps, as displayed in Figure 4b and 5b. As plotted in Figure 4b, without light irradiation (U = 0V), firstly, PE $AgBiP_2Se_6$ monolayer combines with a proton and an electron to form an H* species with an unfavorable ΔG of 1.33 eV; Next, the H* specie continues to bond a proton and an electron to release a H_2 molecule, which is exothermic by 0.54 eV. For FE $AgBiP_2Se_6$ monolayer, the process of hydrogen reduction half reaction is similar, but also with different reaction barriers. The ΔG for the two steps is 1.71 and -0.88eV, respectively, indicating HER is even less favorable at FE phase. Under the external potential (U=0.27 and 0.09 V for PE and FE $AgBiP_2Se_6$ monolayers, respectively) provided by photogenerated electrons, the first step for both cases is still uphill, but the barrier is obviously reduced. For the FE $AgBiP_2Se_6$ monolayer, the barrier is 1.62 eV at pH=7, which is more than 1.5 times of the one (1.06 eV at pH=7) for the PE $AgBiP_2Se_6$ monolayer, indicating the PE phase is more promising for HER although the barrier is still quite high. Generally speaking, HER prefers to react under the acidic environments. When the pH effect is considered, the reaction barrier can be linearly decreased by pH adjustment according to the Equation S11 while the value of U_e can be lifted according to Equation 3. Taken pH=0 as an example, the reaction barrier can be significantly reduced to 0.24 eV (PE) and 0.80 eV (FE) respectively. In order to further decrease the HER barrier, we apply biaxial compression strain, which has been proven as an effective and feasible approach to tune the catalytic activity.[62-64] As illustrated in Figure S8, the formation energy of H* can be reduced with the increase of biaxial compression strain, the value of ΔG_e, *i. e.* the reaction barrier of HER on PE $AgBiP_2Se_6$ monolayer can be effectively lowered (The discussion can be found in the *Supporting Information*). Meanwhile, the value of U_e also can be raised by the biaxial compression strain, due to the lifted CBM as shown in Figure 4e. Therefore, under illumination, the value of ΔG_e drops obviously with the decreasing pH and increasing biaxial compression strain, as displayed in Figure 4f. We set 25 meV as an optimal reaction barrier (the yellow plane),[63] and satisfactorily, there are a large area within the plane, which means the compressed PE $AgBiP_2Se_6$ monolayer could have a high activity for hydrogen production in acid environment. To compare the difference of HER reaction barrier between PE and FE $AgBiP_2Se_6$ monolayer under the same condition, we take the case of pH=1 and -4% biaxial compression strain as an example. As illustrated in Figure 4d and 5d, the HER reaction barrier of PE $AgBiP_2Se_6$ monolayer has reached almost 0 eV under illumination, while the one of FE phase is up to 0.58 eV, demonstrating the ferroelectric switch could also tune the driving force of photogenerated electron of $AgBiP_2Se_6$ monolayer to hydrogen reduction in the acidic environments with aid of strain.

■ CONCLUSIONS

In summary, we theoretically explored the effect of ferroelectric switch on the photocatalytic water-splitting property of $AgBiP_2Se_6$ monolayer by analyzing the difference in structural, electronic, and optical characters between FE and PE phases using comprehensive DFT computations. According to our calculation, the ferroelectric switch could regulate the exciton binding energy, redox abilities and driving force of photogenerated carriers in $AgBiP_2Se_6$ monolayer. More specifically, (i) the PE phase has a stronger reducibility, while the FE phase processes a higher oxidizability; (ii) the driving force of

photogenerated holes of FE $AgBiP_2Se_6$ is stronger than the one in PE phase, while the driving force of photogenerated electron of PE $AgBiP_2Se_6$ is more powerful; (iii) the FE phase has a larger exciton binding energy than PE one, so is monolayer $AgBiP_2S_6$, $CuBiP_2Se_6$ and $CuInP_2S_6$. Our results vividly revealed that the ferroelectric switch is an effective way to modify or improve the 2D ferroelectric photocatalyst. Moreover, FE $AgBiP_2Se_6$ monolayer with strong optical absorbance in visible light region, well H_2O adsorption and oxidation abilities, and adequate driving forces to water oxidation is an ideal photocatalysts for OER. What's more, under biaxial compression strain, the PE $AgBiP_2Se_6$ monolayer could have a high activity for hydrogen production in acid environment.

■ ASSOCIATED CONTENT

Supporting Information.
This material is available free of charge via the Internet at http://pubs.acs.org.
Band structures of PE and FE $AgBiP_2Se_6$ monolayers based on HSE06 with and without the spin-orbit coupling effect; Total and Projected density of states of PE and FE $AgBiP_2Se_6$ monolayers based on HSE06 functional; Imagery parts ε_2 of dielectric functions of PE and FE $AgBiP_2Se_6$, $AgBiP_2S_6$, $CuBiP_2Se_6$ and $CuInP_2S_6$ monolayers based on G_0W_0-BSE level; Band structures of PE and FE $AgBiP_2S_6$, $CuBiP_2Se_6$ and $CuInP_2S_6$ monolayers based on G_0W_0 functional; The H_2O molecule adsorption sites at the PE and FE $AgBiP_2Se_6$ surface; Top and side views of the most stable adsorption structures of H_2O on the surface of PE and FE $AgBiP_2Se_6$ monolayers; The Gibbs free energy changes of OER at different pH on FE $AgBiP_2Se_6$ monolayer under illumination; For the PE $AgBiP_2Se_6$ monolayer, the formation energy of H* under different biaxial compression strains and ΔG_e without illumination under different pH and biaxial compression strains; The direct band gaps at G_0W_0 level, the optical band gaps, exciton binding energies for PE and FE $AgBiP_2S_6$, $CuInP_2S_6$, and $CuBiP_2Se_6$ Monolayers; Details for the solar-to-hydrogen efficiency; Details for Free energy difference; Discussion on the reaction barrier of HER on PE $AgBiP_2Se_6$ monolayer; Details for the thermodynamic oxidation and reduction potentials of PE and FE $AgBiP_2Se_6$ monolayers in aqueous solution. (PDF)

■ AUTHOR INFORMATION

Corresponding Author

* liangzhi.kou@qut.edu.au

Author Contributions

All authors have given approval to the final version of the manuscript.

Notes

The authors declare no competing financial interest.

■ ACKNOWLEDGMENT

This work is supported by National Natural Science foundation of China (Grants No. 11804006), Henan Key Program of Technology Research and Development (No. 182102310907), and Henan College Key Research Project (No. 19A430006). We also acknowledge the grants of high-performance computer time from computing facility at the Queensland University of Technology, the Pawsey Supercomputing Center and Australian National Facility. L.J. gratefully acknowledges China scholarship council for its support (No. 201908410036). L.K. gratefully acknowledges financial support by the ARC Discovery Project (DP190101607).

■ REFERENCES

(1) Liu, Y.-L.; Wu, J. M., Synergistically catalytic activities of $BiFeO_3/TiO_2$ core-shell nanocomposites for degradation of organic dye molecule through piezophototronic effect. *Nano Energy* **2019**, 56, 74-81.
(2) Chen, S.; Ma, G.; Wang, Q.; Sun, S.; Hisatomi, T.; Higashi, T.; Wang, Z.; Nakabayashi, M.; Shibata, N.; Pan, Z.; Hayashi, T.; Minegishi, T.; Takata, T.; Domen, K., Metal selenide photocatalysts for visible-light-driven Z-scheme pure water splitting. *J. Mater. Chem. A* **2019**, 7 (13), 7415-7422.
(3) Pan, L.; Kim, J. H.; Mayer, M. T.; Son, M.-K.; Ummadisingu, A.; Lee, J. S.; Hagfeldt, A.; Luo, J.; Grätzel, M., Boosting the performance of Cu_2O photocathodes for unassisted solar water splitting devices. *Nat. Catal.* **2018**, 1 (6), 412-420.
(4) Fujishima, A.; Honda, K., Electrochemical Photolysis of Water at a Semiconductor Electrode. *Nature* **1972**, 238 (5358), 37-38.
(5) Schneider, J.; Matsuoka, M.; Takeuchi, M.; Zhang, J.; Horiuchi, Y.; Anpo, M.; Bahnemann, D. W., Understanding TiO2 photocatalysis: mechanisms and materials. *Chem. Rev.* **2014**, 114, 9919-86.
(6) Park, T.-Y.; Choi, Y.-S.; Kim, S.-M.; Jung, G.-Y.; Park, S.-J.; Kwon, B.-J.; Cho, Y.-H., Electroluminescence emission from light-emitting diode of p-ZnO/(InGaN/GaN) multiquantum well/n-GaN. *Appl. Phys. Lett.* **2011**, 98, 251111.
(7) Cardona, M., Optical Properties and Band Structure of $SrTiO_3$ and $BaTiO_3$. *Phys. Rev.* **1965**, 140, A651-A655.
(8) Kudo, A.; Miseki, Y., Heterogeneous photocatalyst materials for water splitting. *Chem. Soc. Rev.* **2009**, 38, 253-78.
(9) Ju, L.; Dai, Y.; Wei, W.; Liang, Y.; Huang, B., Potential of one-dimensional blue phosphorene nanotubes as a water splitting photocatalyst. *J. Mater. Chem. A* **2018**, 6, 21087-21097.
(10) Meng, R.; Sun, X.; Yang, D.; Bao, J.; Chen, X., Two dimensional XAs (X = Si, Ge, Sn) monolayers as promising photocatalysts for water splitting hydrogen production with high carrier mobility. *Appl. Mater. Today* **2018**, 13, 276-284.
(11) Ji, Y.; Dong, H.; Hou, T.; Li, Y., Monolayer graphitic germanium carbide (g-GeC): the promising cathode catalyst for fuel cell and lithium–oxygen battery applications. *J. Mater. Chem. A* **2018**, 6, 2212-2218.
(12) Qiao, M.; Chen, Y.; Wang, Y.; Li, Y., The germanium telluride monolayer: a two dimensional semiconductor with high carrier mobility for photocatalytic water splitting. *J. Mater. Chem. A* **2018**, 6, 4119-4125.
(13) Mao, Y.; Guo, G.; Yuan, J.; Zhong, J., Edge-doping effects on the electronic and magnetic properties of zigzag germanium selenide nanoribbon. *Appl. Surf. Sci.* **2019**, 464, 236-242.
(14) Fang, Q.; Zhao, X.; Huang, Y.; Xu, K.; Min, T.; Chu, P. K.; Ma, F., Interfacial electronic states and self-formed p–n junctions in hydrogenated MoS_2/SiC heterostructure. *J. Mater. Chem. C* **2018**, 6, 4523-4530.
(15) Kumar, R.; Das, D.; Singh, A. K., C_2N/WS_2 van der Waals type-II heterostructure as a promising water splitting photocatalyst. *J. Catal.* **2018**, 359, 143-150.
(16) Fan, Y.; Ma, X.; Liu, X.; Wang, J.; Ai, H.; Zhao, M., Theoretical Design of an InSe/GaTe vdW Heterobilayer: A Potential Visible-Light Photocatalyst for Water Splitting. *J. Phys. Chem. C* **2018**, 122,

27803-27810.
(17) Zhao, P.; Ma, Y.; Lv, X.; Li, M.; Huang, B.; Dai, Y., Two-dimensional III_2-VI_3 materials: Promising photocatalysts for overall water splitting under infrared light spectrum. *Nano Energy* **2018**, 51, 533-538.
(18) Ma, X.; Wu, X.; Wang, H.; Wang, Y., A Janus MoSSe monolayer: a potential wide solar-spectrum water-splitting photocatalyst with a low carrier recombination rate. *J. Mater. Chem. A* **2018**, 6, 2295-2301.
(19) Liu, Y.; Zeng, X.; Hu, X.; Hu, J.; Wang, Z.; Yin, Y.; Sun, C.; Zhang, X., Two-dimensional g-C_3N_4/TiO_2 nanocomposites as vertical Z-scheme heterojunction for improved photocatalytic water disinfection. *Catal. Today* **2019**, 335, 243-251.
(20) Cao, A.; Zhang, L.; Wang, Y.; Zhao, H.; Deng, H.; Liu, X.; Lin, Z.; Su, X.; Yue, F., 2D–2D Heterostructured UNiMOF/g-C_3N_4 for Enhanced Photocatalytic H_2 Production under Visible-Light Irradiation. *ACS Sustain. Chem. Eng.* **2018**, 7, 2492-2499.
(21) Wang, W.; Zhang, H.; Zhang, S.; Liu, Y.; Wang, G.; Sun, C.; Zhao, H., Potassium Ion Assisted Regeneration of Active Cyano Groups in Carbon Nitride Nanoribbons: Visible Light Driven Photocatalytic Nitrogen Reduction. *Angew. Chem. Int. Ed. Engl.* **2019**, 58 (46), 16644-16650.
(22) Tan, B.; Ye, X.; Li, Y.; Ma, X.; Wang, Y.; Ye, J., Defective Anatase TiO_{2-x} Mesocrystal Growth In Situ on g-C_3N_4 Nanosheets: Construction of 3D/2D Z-Scheme Heterostructures for Highly Efficient Visible-Light Photocatalysis. *Chem.* **2018**, 24 (50), 13311-13321.
(23) Jing, Y.; Ma, Y.; Wang, Y.; Li, Y.; Heine, T., Ultrathin Layers of PdPX (X=S, Se): Two Dimensional Semiconductors for Photocatalytic Water Splitting. *Chem.* **2017**, 23 (55), 13612-13616.
(24) Jing, Y.; Heine, T., Two-dimensional $Pd_3P_2S_8$ semiconductors as photocatalysts for the solar-driven oxygen evolution reaction: a theoretical investigation. *J. Mater. Chem. A* **2018**, 6, 23495-23501.
(25) Ju, L.; Dai, Y.; Wei, W.; Li, M.; Jin, C.; Huang, B., Theoretical study on the photocatalytic properties of graphene oxide with single Au atom adsorption. *Surf. Sci.* **2018**, 669, 71-78.
(26) Jin, C.; Dai, Y.; Wei, W.; Ma, X.; Li, M.; Huang, B., Effects of single metal atom (Pt, Pd, Rh and Ru) adsorption on the photocatalytic properties of anatase TiO_2. *Appl. Surf. Sci.* **2017**, 426, 639-646.
(27) Zhu, Z.; Yin, H.; He, C. T.; Al-Mamun, M.; Liu, P.; Jiang, L.; Zhao, Y.; Wang, Y.; Yang, H. G.; Tang, Z.; Wang, D.; Chen, X. M.; Zhao, H., Ultrathin Transition Metal Dichalcogenide/3d Metal Hydroxide Hybridized Nanosheets to Enhance Hydrogen Evolution Activity. *Adv. Mater.* **2018**, 30, e1801171.
(28) Qi, Y.; Xu, Q.; Wang, Y.; Yan, B.; Ren, Y.; Chen, Z., CO_2-Induced Phase Engineering: Protocol for Enhanced Photoelectrocatalytic Performance of 2D MoS_2 Nanosheets. *ACS Nano* **2016**, 10, 2903-9.
(29) Liu, B.; Wang, Y.; Peng, H. Q.; Yang, R.; Jiang, Z.; Zhou, X.; Lee, C. S.; Zhao, H.; Zhang, W., Iron Vacancies Induced Bifunctionality in Ultrathin Feroxyhyte Nanosheets for Overall Water Splitting. *Adv. Mater.* **2018**, e1803144.
(30) He, X.; Li, H.; Zhu, Z.; Dai, Z.; Yang, Y.; Yang, P.; Zhang, Q.; Li, P.; Schwingenschlogl, U.; Zhang, X., Strain engineering in monolayer WS_2, MoS_2, and the WS_2/MoS_2 heterostructure. *Appl. Phys. Lett.* **2016**, 109, 173105.
(31) Ju, L.; Dai, Y.; Wei, W.; Li, M.; Liang, Y.; Huang, B., One-dimensional cadmium sulphide nanotubes for photocatalytic water splitting. *Phys. Chem. Chem. Phys.* **2018**, 20, 1904-1913.
(32) Gu, D.; Tao, X.; Chen, H.; Zhu, W.; Ouyang, Y.; Peng, Q., Enhanced photocatalytic activity for water splitting of blue-phase GeS and GeSe monolayers via biaxial straining. *Nanoscale* **2019**, 11, 2335-2342.
(33) Ju, L.; Dai, Y.; Wei, W.; Li, M.; Huang, B., DFT investigation on two-dimensional GeS/WS_2 van der Waals heterostructure for direct Z-scheme photocatalytic overall water splitting. *Appl. Surf. Sci.* **2018**, 434, 365-374.
(34) Yang, H.; Ma, Y.; Zhang, S.; Jin, H.; Huang, B.; Dai, Y., GeSe@SnS: stacked Janus structures for overall water splitting. *J. Mater. Chem. A* **2019**, 7, 12060-12067.
(35) Alexe, M.; Ziese, M.; Hesse, D.; Esquinazi, P.; Yamauchi, K.; Fukushima, T.; Picozzi, S.; Gösele, U., Ferroelectric Switching in Multiferroic Magnetite (Fe_3O_4) Thin Films. *Adv. Mater.* **2009**, 21, 4452-4455.
(36) Di Sante, D.; Stroppa, A.; Jain, P.; Picozzi, S., Tuning the ferroelectric polarization in a multiferroic metal-organic framework. *J. Am. Chem. Soc.* **2013**, 135, 18126-30.
(37) Rinaldi, C.; Varotto, S.; Asa, M.; Slawinska, J.; Fujii, J.; Vinai, G.; Cecchi, S.; Di Sante, D.; Calarco, R.; Vobornik, I.; Panaccione, G.; Picozzi, S.; Bertacco, R., Ferroelectric Control of the Spin Texture in GeTe. *Nano Lett.* **2018**, 18, 2751-2758.
(38) Stroppa, A.; Di Sante, D.; Barone, P.; Bokdam, M.; Kresse, G.; Franchini, C.; Whangbo, M. H.; Picozzi, S., Tunable ferroelectric polarization and its interplay with spin-orbit coupling in tin iodide perovskites. *Nat. Commun.* **2014**, 5, 5900.
(39) Jain, P.; Stroppa, A.; Nabok, D.; Marino, A.; Rubano, A.; Paparo, D.; Matsubara, M.; Nakotte, H.; Fiebig, M.; Picozzi, S.; Choi, E. S.; Cheetham, A. K.; Draxl, C.; Dalal, N. S.; Zapf, V. S., Switchable electric polarization and ferroelectric domains in a metal-organic-framework. *npj Quantum Mater.* **2016**, 1, 16012.
(40) Li, X.; Li, Z.; Yang, J., Proposed photosynthesis method for producing hydrogen from dissociated water molecules using incident near-infrared light. *Phys. Rev. Lett.* **2014,** *112* (1), 018301.
(41) Sun, Z.-Z.; Xun, W.; Jiang, L.; Zhong, J.-L.; Wu, Y.-Z., Strain engineering to facilitate the occurrence of 2D ferroelectricity in $CuInP_2S_6$ monolayer. *J. Phys. D: Appl. Phys.* **2019**, 52, 465302.
(42) Qi, J.; Wang, H.; Chen, X.; Qian, X., Two-dimensional multiferroic semiconductors with coexisting ferroelectricity and ferromagnetism. *Appl. Phys. Lett.* **2018**, 113, 043102.
(43) Kresse, G.; Furthmüller, J., Efficient iterative schemes for ab initio total-energy calculations using a plane-wave basis set. *Phys. Rev. B* **1996**, 54, 11169-11186.
(44) Kresse, G.; Furthmüller, J., Efficiency of ab-initio total energy calculations for metals and semiconductors using a plane-wave basis set. *Comput. Mater. Sci.* **1996**, 6, 15-50.
(45) Blöchl, P. E., Projector augmented-wave method. *Phys. Rev. B* **1994**, 50, 17953-17979.
(46) Kresse, G.; Joubert, D., From ultrasoft pseudopotentials to the projector augmented-wave method. *Phys. Rev. B* **1999**, 59, 1758-1775.
(47) Perdew, J. P.; Burke, K.; Ernzerhof, M., Generalized Gradient Approximation Made Simple. *Phys. Rev. Lett.* **1996**, 77, 3865-3868.
(48) Heyd, J.; Scuseria, G. E.; Ernzerhof, M., Hybrid functionals based on a screened Coulomb potential. *J. Chem. Phys.* **2003**, 118, 8207-8215.
(49) Grimme, S., Semiempirical GGA-type density functional constructed with a long-range dispersion correction. *J. Comput. Chem.* **2006**, 27, 1787-99.
(50) Mao, X.; Kour, G.; Zhang, L.; He, T.; Wang, S.; Yan, C.; Zhu, Z.; Du, A., Silicon-doped graphene edges: an efficient metal-free catalyst for the reduction of CO_2 into methanol and ethanol. *Catal. Sci. Technol.* **2019,** *9* (23), 6800-6807.
(51) Mathew, K.; Sundararaman, R.; Letchworth-Weaver, K.; Arias, T. A.; Hennig, R. G., Implicit solvation model for density-functional study of nanocrystal surfaces and reaction pathways. *J. Chem. Phys.* **2014,** *140* (8), 084106.
(52) Zhang, C.; Nie, Y.; Du A., Intrinsic Ultrahigh Negative Poisson's Ratio in Two-Dimensional Ferroelectric ABP_2X_6 Materials. *Acta Phys. -Chim. Sin.* **2019**, 35, 1128-1133.

(53) Xu, B.; Xiang, H.; Xia, Y.; Jiang, K.; Wan, X.; He, J.; Yin, J.; Liu, Z., Monolayer $AgBiP_2Se_6$: an atomically thin ferroelectric semiconductor with out-plane polarization. *Nanoscale* **2017**, 9, 8427-8434.
(54) Neugebauer, J.; Scheffler, M., Adsorbate-substrate and adsorbate-adsorbate interactions of Na and K adlayers on Al(111). *Phys. Rev. B: Condens. Matter.* **1992**, 46, 16067-16080.
(55) Choi, J. H.; Cui, P.; Lan, H.; Zhang, Z., Linear Scaling of the Exciton Binding Energy versus the Band Gap of Two-Dimensional Materials. *Phys. Rev. Lett.* **2015**, 115, 066403.
(56) Jiang, Z.; Liu, Z.; Li, Y.; Duan, W., Scaling Universality between Band Gap and Exciton Binding Energy of Two-Dimensional Semiconductors. *Phys. Rev. Lett.* **2017**, 118, 266401.
(57) Qiao, M.; Liu, J.; Wang, Y.; Li, Y.; Chen, Z., $PdSeO_3$ Monolayer: Promising Inorganic 2D Photocatalyst for Direct Overall Water Splitting Without Using Sacrificial Reagents and Cocatalysts. *J. Am. Chem. Soc.* **2018**, 140, 12256-12262.
(58) Fu, C.-F.; Luo, Q.; Li, X.; Yang, J., Two-dimensional van der Waals nanocomposites as Z-scheme type photocatalysts for hydrogen production from overall water splitting. *J. Mater. Chem. A* **2016**, 4, 18892-18898.
(59) Chen, S.; Wang, L.-W., Thermodynamic Oxidation and Reduction Potentials of Photocatalytic Semiconductors in Aqueous Solution. *Chem. Mater.* **2012**, 24, 3659-3666.
(60) Fu, C. F.; Sun, J.; Luo, Q.; Li, X.; Hu, W.; Yang, J., Intrinsic Electric Fields in Two-dimensional Materials Boost the Solar-to-Hydrogen Efficiency for Photocatalytic Water Splitting. *Nano Lett.* **2018**, 18, 6312-6317.
(61) Jamesh, M.-I.; Sun, X., Recent progress on earth abundant electrocatalysts for oxygen evolution reaction (OER) in alkaline medium to achieve efficient water splitting – A review. *J. Power Sources* **2018,** *400*, 31-68.
(62) Xue, X.; Zang, W.; Deng, P.; Wang, Q.; Xing, L.; Zhang, Y.; Wang, Z. L., Piezo-potential enhanced photocatalytic degradation of organic dye using ZnO nanowires. *Nano Energy* **2015,** *13*, 414-422.
(63) Er, D.; Ye, H.; Frey, N. C.; Kumar, H.; Lou, J.; Shenoy, V. B., Prediction of Enhanced Catalytic Activity for Hydrogen Evolution Reaction in Janus Transition Metal Dichalcogenides. *Nano Lett.* **2018,** *18* (6), 3943-3949.
(64) Feng, H.; Xu, Z.; Wang, L.; Yu, Y.; Mitchell, D.; Cui, D.; Xu, X.; Shi, J.; Sannomiya, T.; Du, Y.; Hao, W.; Dou, S. X., Modulation of Photocatalytic Properties by Strain in 2D BiOBr Nanosheets. *ACS Appl. Mater. Interfaces* **2015,** *7* (50), 27592-6.

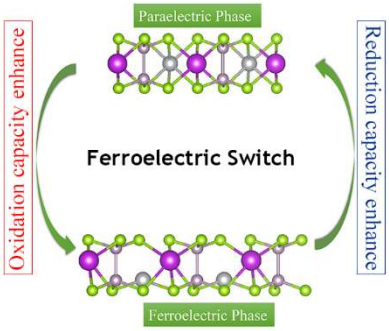

Table of Contents